



## Experimental study of the mechanism of prepulse current on Z-pinch plasma using Faraday rotation diagnosis

Zhiyuan Jiang, Jian Wu ,\* Ziwei Chen, Wei Wang, Zhenyu Wang , Yuanbo Lu, Yiming Zhao, Huantong Shi, and Xingwen Li

State Key Laboratory of Electrical Insulation and Power Equipment, Xi'an Jiaotong University, Xi'an, Shaanxi Province 710049, China



(Received 11 January 2023; accepted 10 April 2023; published 3 May 2023)

The prepulse current is an effective way to optimize the load structure and improve the implosion quality of the Z-pinch plasma. Investigating the strong coupling between the preconditioned plasma and pulsed magnetic field is essential for the design and improvement of prepulse current. In this study, the mechanism of the prepulse current on the Z-pinch plasma was revealed by determining the two-dimensional magnetic field distribution of preconditioned and nonpreconditioned single-wire Z-pinch plasma with a high-sensitivity Faraday rotation diagnosis. When the wire was nonpreconditioned, the current path was consistent with the plasma boundary. When the wire was preconditioned, the distributions of current and mass density presented good imploding axial uniformity, and the imploding speed of the current shell was higher than that of the mass shell. In addition, the mechanism of the prepulse current suppressing the magneto-Rayleigh-Taylor instability was revealed, which formed a sharp density profile of the imploding plasma and slowed the shock wave driven by the magnetic pressure. This discovery is essential and instructive for the design of preconditioned wire-array Z-pinch experiments.

DOI: [10.1103/PhysRevE.107.055201](https://doi.org/10.1103/PhysRevE.107.055201)

### I. INTRODUCTION

Z pinch is a process that involves the implosion of a cylindrical plasma that is subject to a radial  $\mathbf{J} \times \mathbf{B}$  force derived from a pulsed current. This process is considered as the most effective method for simulating a strong pulsed soft x-ray radiation environment in the laboratory, with potential applications in areas such as inertial confinement fusion, laboratory astrophysics, and high-energy-density physics [1–5]. To achieve a stagnant state with high density and temperature, it is essential to maintain symmetry and stability during the implosion process of the Z-pinch plasma. However, the emergence of the magneto-Rayleigh-Taylor instability (MRTI) significantly undermines the quality of the implosion [6].

Mass density regulation has been suggested and implemented to enhance stability during the implosion process. The use of a prepulse current, which involves a small current pulse before the main current, has proven to be an effective method for optimizing the load structure and improving implosion quality [7]. Lorenz *et al.* [8] used a prepulse current (10 kA, 180 ns) to preheat a carbon fiber Z pinch, and found that a prepulse current can delay the implosion time and increase the x-ray yield and electron temperature. Harvey-Thompson *et al.* used a two-stage linear array configuration to introduce a prepulse current in the Z-pinch experiment of a cylindrical aluminum linear array. Preconditioning can suppress the ablation stage and axial inhomogeneity [7,9]. Furthermore, experiments involving one-wire, two-wire, and wire-array Z

pinch were carried out on the “Qin-1” facility, a double-pulse current generator used to investigate the dynamics of preconditioned load [10,11]. The influence of the time delay between the prepulse and main current on the mass distribution was also experimentally studied.

However, prior studies on preconditioned Z-pinch plasma have mainly focused on plasma density distribution, dynamic behavior, and instability changes. The strong coupling between the plasma and pulsed magnetic field is a key problem in Z-pinch plasma, and serves as the basis for further improving the quality of Z-pinch implosion [12–17]. The specific mechanism by which the prepulse current affects magnetic field and mass distribution, thereby altering the dynamic behavior in Z-pinch plasma, has not yet been fully understood.

This study focused on investigating the two-dimensional (2D) magnetic field distributions of preconditioned and nonpreconditioned single-wire Z-pinch plasmas using Faraday rotation diagnosis. The current distributions at different radii were calculated and analyzed under two distinct conditions. Additionally, the study discussed the impact of the prepulse current on implosion dynamics and plasma parameters.

### II. EXPERIMENTAL SETUP

The experiments were carried out on the Qin-1 pulsed generator (450 kA, 400 ns) at Xi'an Jiaotong University. The generator featured an independently triggered prepulse current generator (15 kA, 40 ns) [18]. The time-resolved dynamic behaviors of the Z-pinch plasma were recorded through laser shadowgraphy diagnostics using a streak camera and a continuous laser. During the experiments, a 532-nm laser

\*jxjawj@mail.xjtu.edu.cn

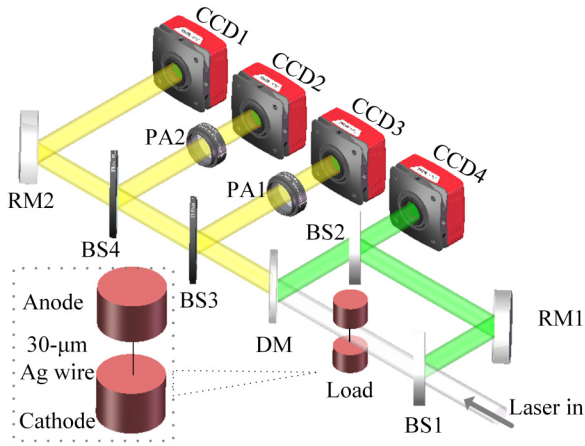


FIG. 1. Experimental setup for shadowgraphy (CCD1), Faraday rotation (CCD2, CCD3), and interferometry (CCD4). CCD: Charge-coupled device; PA: Polarization analyzer; DM: Dichroic mirror; RM: Reflect mirror; BS: Beam splitter. The enlarged part is the structure of the load consisting of an anode, a single wire, and a cathode.

was utilized for the Mach-Zehnder interferometer to measure the electron density [19]. A 1064-nm laser was employed for Faraday rotation and shadowgraphy, as shown in Fig. 1.

Two Faraday channels and one shadowgraphy channel were constructed using two nonpolarized beam splitters and one reflector. The Faraday channels were analyzed using high extinction ratio polarizers (LPVIS100-MP2; Thorlabs) to measure the Faraday rotation distribution [20]. Furthermore,

a second polarization of the probe laser was achieved by exploiting the distinct reflectance or transmission efficiencies of the *p* and *s* components as they pass through the beam splitters. This conversion of the original small rotation angle into a larger angle increased the measurement sensitivity of the Faraday rotation [21].

### III. EXPERIMENTAL RESULTS

Z-pinch experiments involved using a single 30- $\mu\text{m}$  silver wire with a height of 2 cm. The results obtained with and without the prepulse current are presented in Fig. 2, including the electrical signals and streak camera images. The shadowgraphy images at different moments from distinct shots are shown in Fig. 3. When only the main current was applied to the load, the wire expanded first and then imploded slightly at around 150 ns according to the streak camera image. The x-ray signal was measured at approximately 210 ns along with no implosion observed from the streak camera. It indicated that the implosion was axially inhomogeneous and was consistent with shadowgraphy images. The 2D shadowgraph images showed the sausage structure with imploding and nonimploding regions along the axial direction. It was related to different initial heating rates at the axial locations, which would cause a slight fluctuation in thickness at various positions along the axial axis.

When a prepulse current was applied to the load, the wire underwent heating and vaporization, eventually forming a core-coronal structure. The wire core experienced unconstrained expansion with a velocity of approximately 3 km/s.

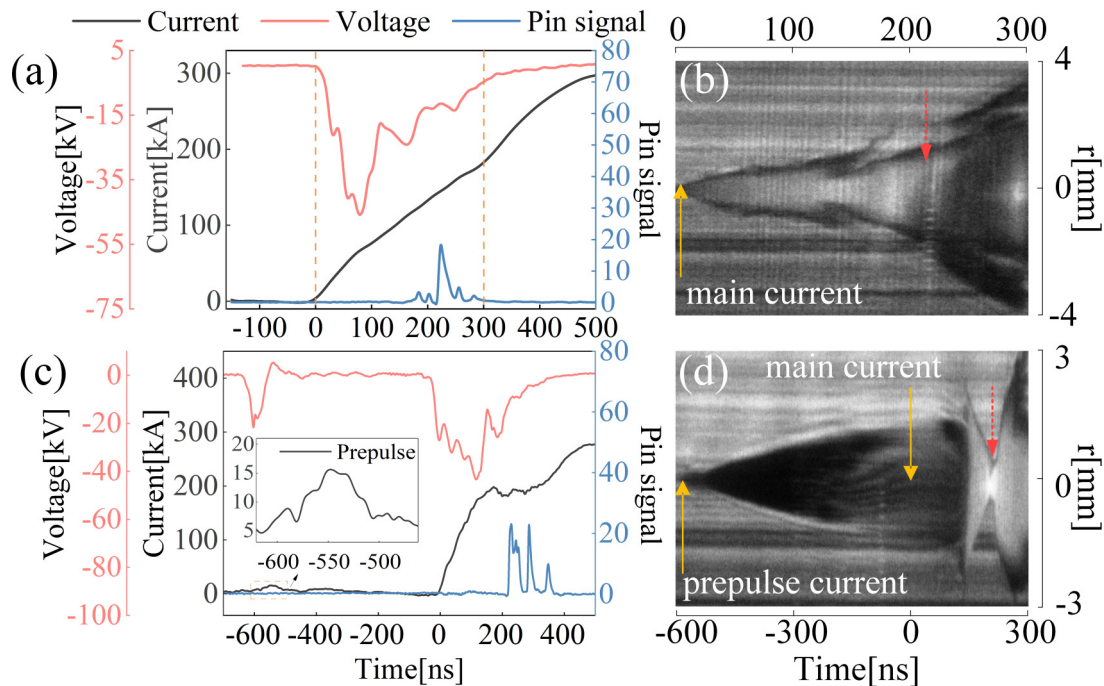


FIG. 2. (a), (c) Waveform of current (gray), voltage (red), and pin signal (blue) of a single wire Z pinch without the prepulse current (shot No. 220331) and with the prepulse current (shot No. 220340), respectively. The x axis represents time, and the time of the main current is 0. The enlarged picture shows the prepulse current. (b), (d) Captured streak cameras image of 30- $\mu\text{m}$  single silver wire in shot No. 220331 and shot No. 220340, respectively. The yellow solid lines with arrows mean the moment of applied current and the red solid lines with arrows mean the moment of radiation. The x axis represents time while the y axis represents radius. The original location of the wire is  $r = 0$ .

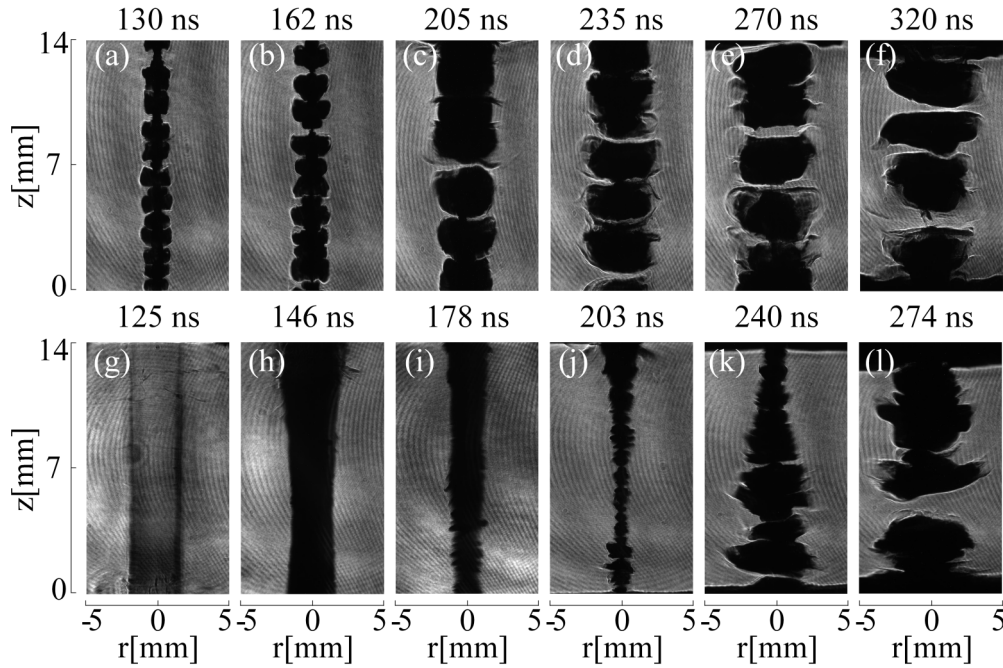


FIG. 3. (a)–(f) Shadowgraphy images captured from different shots when only the main current was applied. The numbers indicate the time interval between the photo moment and the main current: (a) 130 ns—No. 220330, (b) 162 ns—No. 220331, (c) 205 ns—No. 220334, (d) 235 ns—No. 220335, (e) 270 ns—No. 220333, and (f) 235 ns—No. 220336. (g)–(l) Shadowgraphy images captured from different shots when the prepulse current and main current were applied. The numbers indicate the time interval between the photo moment and the main current: (g) 125 ns—No. 220340, (h) 146 ns—No. 220343, (i) 178 ns—No. 220312, (j) 203 ns—No. 220337, (k) 240 ns—No. 220327, and (l) 274 ns—No. 220322. The longitudinal and horizontal axes in these images represent the  $z$  axis and radius, respectively.

The coronal plasma expanded at a higher and indiscernible velocity. The time interval between the main pulse and the prepulse is 600 ns. Once the primary current was initiated, the expanding coronal plasma experienced a deceleration and implosion. The compressed coronal plasma transformed into a dense shell, exhibiting snowplow implosion characteristics, which were observed at around 130 ns. The dense shell and the wire core collided and imploded in unison, finally coming to a stagnation at approximately 210 ns. According to shadowgraphy images shown in Figs. 3(g)–3(i), there is almost no MRTI in the early stages of implosion. After 170 ns, the instability emerged, with an amplitude of approximately 0.1–0.3 mm. At 203 ns, the amplitude increased to 0.3–0.6 mm and subsequently grew rapidly, reaching an amplitude of approximately 0.8–1.5 mm by 240 ns. Overall, the amplitude of the MRTI exhibited exponential growth throughout its development.

Figure 4 presents the typical results of the Faraday images, shadowgraphy images, and interferometry obtained during shot No. 220330 at  $t = 130$  ns when only the main current was applied. Measurements of the electron density and Faraday rotation at the edge of the nonimploding region enabled the calculation of the magnetic field. The magnetic field was measured to be 8 T at  $r = 0.5$  mm, indicating that the current inside the dense shell was approximately 22 kA, which accounted for less than 20% of the total current. The remaining 80 kA of current was mainly distributed in the radial range of 0.57–0.94 mm, with a width of approximately 0.4 mm. The use of laser interferometry was unable to measure the electron density at the edge of the imploding or neck region, suggesting that the current sheath was located within the plasma column.

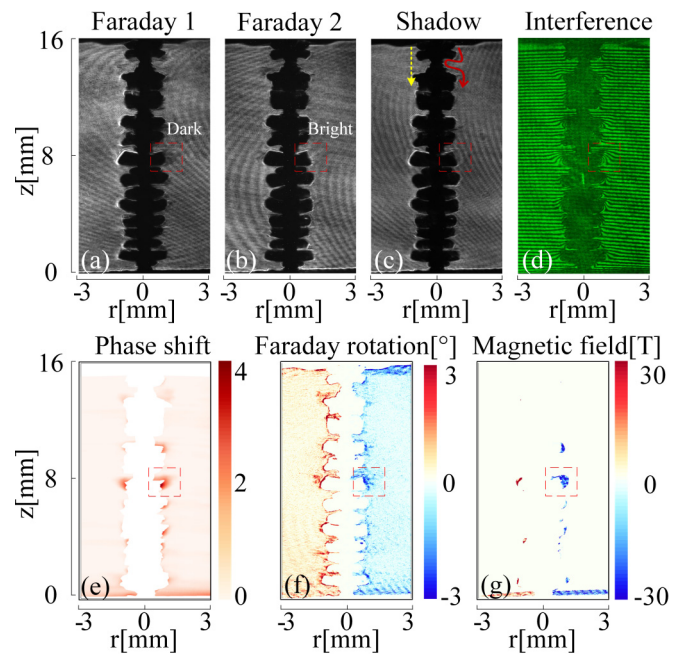


FIG. 4. The measured results of Faraday diagnosis at  $t = 130$  ns in shot No. 220330, including (a) Faraday image in Faraday channel 1, (b) Faraday image in Faraday channel 2, (c) shadowgraphy image, (d) interference image and calculated distribution of (e) phase shift, (f) Faraday rotation ( $^{\circ}$ ), and (g) magnetic field (T). The load was a 30- $\mu$ m single silver wire with a height of 2 cm. Different colors in (e)–(g) represent the amplitude of corresponding parameters. The horizontal and longitudinal axes represent the radius and the  $z$  axis, separately.



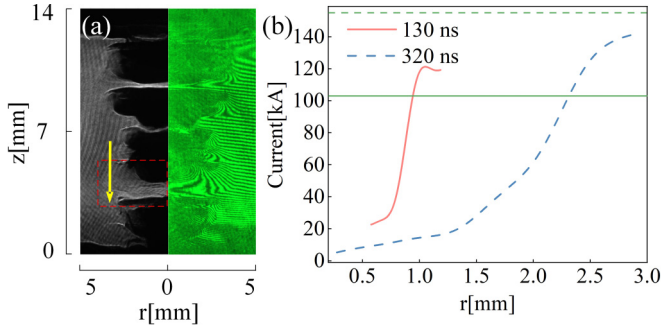


FIG. 5. (a) The measured results of shadowgraphy and interferometry at  $t = 320$  ns when solely the main pulse was applied. The shadow images and interference images are symmetrical about the axis. The horizontal and longitudinal axes represent the radius and the  $z$  axis, respectively. (b) Calculated averaged value of current at different radii in the dashed red frame in Fig. 4(a) at  $t = 130$  ns and in Fig. 5(a) at  $t = 320$  ns. The solid and dashed green lines represent the current measured by the Rogowski coil at 130 and 320 ns, respectively.

Notably, the current connection between the imploding and nonimploding regions indicated a zipperlike structure of the current path.

Furthermore, the dissimilarity between the imploding and nonimploding regions can be elucidated by examining the current distribution profiles. Specifically, the imploding region possesses a thinner current sheath and smaller radius, resulting in a larger  $\mathbf{J} \times \mathbf{B}$  force. Assuming a sheath thickness of 0.1 mm for the imploding region, the total Lorentz force of the imploding plasma region was 67.8% greater than that of the nonimploding region [22]. This axial discrepancy was caused by the varying distribution radii of the current, which can be attributed to the disturbed initial heating of the wire at different positions.

In Fig. 5(a), the plasma image after stagnation at  $t = 320$  ns is depicted, where the imploding area results in a disconnection between the expanding plasma. It is interesting to understand the current path with the gaps in this region.

The electron density and magnetic field distributions were detectable at this moment, and the results showed that 70% of the total current was mainly distributed beyond a radius of 1.8 mm, which was the same as the radius of the adjacent expanding area. Therefore, it can be inferred that the current path was consistent with the yellow solid line shown in Fig. 5(a). In Fig. 5 (b), a comparison of the current distribution between the current shell during the implosion process and the disconnected region after stagnation is presented. It can be observed that the current would redistribute from a smaller radius to a larger radius in this process, which is likely caused by the change of electron density.

When the wire was preconditioned, the shadowgraphy and interference images of two typical phases including implosion and stagnation were shown in Fig. 6. In the implosion phase, an axially uniform plasma column was formed and a current shell with a width of 1 mm was detected on the outer surface of the plasma at 125 ns after the main current, as illustrated in Fig. 6(a). The plasma exhibited no notable MRTI and underwent implosion, leading to the formation of a dense shell with a distinct boundary in the shadowgraphy image. The phase shift in the interference image was chiefly concentrated at the boundary of the dense shell, with a maximum phase shift of 1.9, corresponding to an areal electron density of  $8 \times 10^{17} \text{ cm}^{-2}$ . Furthermore, the findings indicated that 60% of the total current was occupied by the plasma outside the dense shell.

In the stagnation phase, the shadowgraphy image at 203 ns is shown in Fig. 6(b). The minimum radius of the high-density plasma was 0.3 mm and the implosion mass had significantly improved compared to the condition without the main current. The interference images revealed that the electron density on the surface of the high-density plasma was insufficient to present a noticeable phase shift. These results indicate that the current was more concentrated in the stagnation phase, and the current in most axial areas was distributed on the surface of the stagnant plasma.

Additionally, the development of MRTI results in measurable areal electron densities in some areas. The Faraday

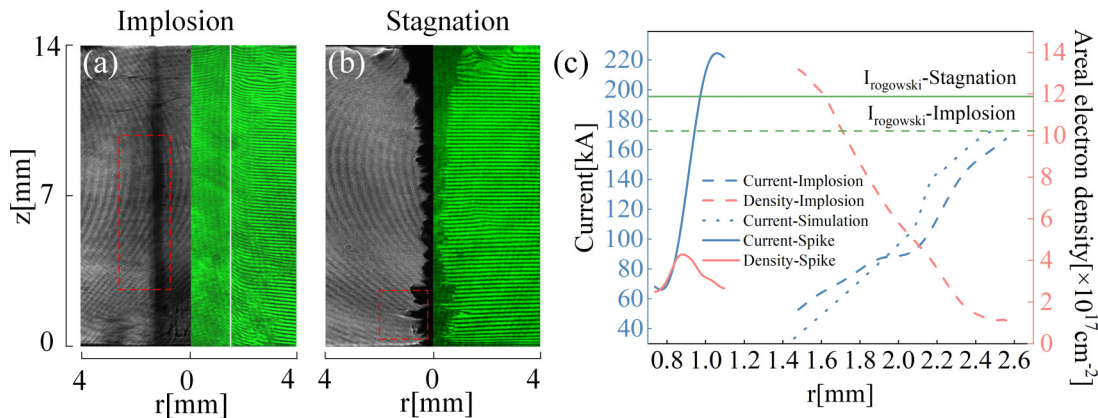


FIG. 6. (a),(b) The measured results of shadowgraphy and interference images during implosion ( $t = 125$  ns, shot No. 220340) and stagnation ( $t = 203$  ns, shot No. 220337), respectively, when both the prepulse and the main pulse were applied. The white line in (a) represents the dense shell. Shadowgraphy and interference images are symmetrical about the axis. (c) Calculated averaged current and areal electron density at different radii within the dashed red frames in (a) and (b). The dotted line represents the simulated results at  $t = 125$  ns using Helios [23]. The dashed and solid green lines represent the current measured by the Rogowski coil at  $t = 125$  and 203 ns, respectively.

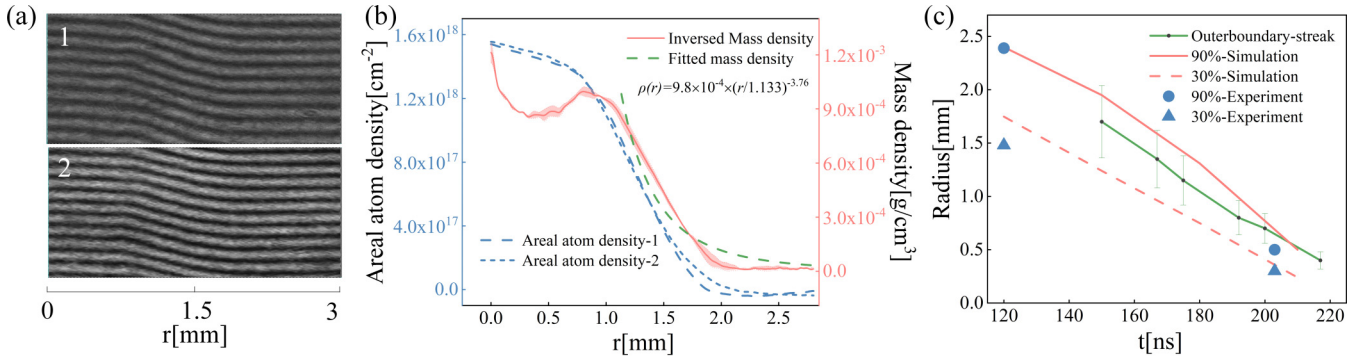


FIG. 7. (a) The example of interference images from two directions. (b) The measured areal atom density of interference 1 (blue dashed curve) and interference 2 (blue dotted curve) when the time interval of prepulse current and photograph is 600 ns. The solid red line represents calculated mass density using Abel inversion and the error is caused by slight azimuthal asymmetry. The dashed green line represents the fitted line of calculated mass density when  $r > 1.13$  mm. (c) Calculated results of the Helios compared with the experimentally measured results. The ratio means the percentage of internal current inside the radius where it is located to total current. The red solid curve represents the radius of the boundary of the 90% current while the red dashed curve represents the radius of the boundary of the 30% current of the simulation results. The blue round dots represent the radii of the boundary of the 90% current while the blue triangle dots represent the radius of the boundary of the 30% current of the experimental results. The green line shows the boundary of streak camera image.

diagnostic results for this “spike” area revealed that most of the current is located within a radius of 0.8–1.05 mm. Figure 6(c) shows the current distribution of the imploding area in the implosion and of the “spike” area at stagnation. Assuming the cylindrical structure of the plasma, in the imploding phase, averaged current density in the radial range of 1.5–2.5 mm is 8.75 kA/mm<sup>2</sup>. In the stagnation phase, the current density in the radial range of 0.8–1.05 mm is 106.68 kA/mm<sup>2</sup>. Therefore, the current density on the surface of the high-density plasma increased significantly during the implosion process.

#### IV. DISCUSSION

In the initial stages of implosion, the plasma column did not display obvious MRTI. To explore the suppression of instability, the areal atom density of the preconditioned Ag wire was measured using two interferometers, with the angle between them set at 45° to ensure cylindrical symmetry. Abel inversion was employed with a Fourier series [23] and the calculated mass density is shown in Fig. 7(a). The density profile changed rapidly beyond the radius of 1.13 mm according to the fitted line with a 95% confidence interval. This density is consistent with the power-law density profile [24,25]. This stratified plasma layer slows down the shock wave driven by the magnetic pressure and outer interface simultaneously, which is also consistent with the decrease in implosion acceleration shown in the streak camera image. This implies that the effective gravity vector  $\mathbf{g}$  is directed from the magnetic field (massless fluid) to the plasma, thus suppressing the development of MRTI in the early stage of implosion. Concurrently, there are stratification structures that likely arise from resistivity perturbations during the explosion and provide initial seeds for instability development [26]. Therefore, when the radius of the plasma column was smaller than 1.13 mm, the MRTI could not be suppressed by the density profile and began a rapid development.

In order to gain a deeper understanding of the implosion process with preconditioning, the Helios was employed

to calculate the implosion process of the core-coronal structure using a one-dimensional and two-temperature resistive magnetohydrodynamics model [27]. Radiation multi-group diffusion under a cylindrical coordinate Lagrangian grid was adopted. The equations of state and opacity were computed with the PRISM-PROPACEOS 8.0.0 program, while the Spitzer model was employed to determine thermal conductivity and resistivity. The initial density profile was substituted with the fitted results shown in Fig. 7(b). The calculated current distribution during the implosion stage aligned well with the measured results in Fig. 6(c). Detailed results of the current distribution are shown in Fig. 7(c). The current shell shows a trend similar to that of the outer plasma shell observed in the streak camera image. The velocity of implosion surpassed that of the plasma shell, causing an increase in current density. Interestingly, our findings reveal no evidence of current redistribution at stagnation which was observed in gas-puff and wire-array Z pinches [28–30]. This observation could be attributed to the fact that, following preconditioning, the majority of mass is involved in the implosion process, thereby leading to an extremely low plasma density and a substantial resistivity outside the stagnated plasma.

The error in this experiment can be attributed to two main factors. The first factor is the impact of azimuthal asymmetry and plasma instability on the magnetic field and current distribution. Through analyzing the azimuthal asymmetry in the implosion process using two-angle shadowgraph, it was found that the average error of the radius was 3% with the prepulse and 11% without the prepulse. The second factor is the fluctuation in the laser energy. An index computed from the intensity of the captured images was utilized to determine the rotation distribution. Therefore, it is crucial to accurately determine the relationship between the rotation angle  $\alpha$  and the index. For this purpose, a polarizer was employed for calibration. The measured value of the index at each pixel exhibited some variation within a particular range when the simulated rotation angle was the same. The pixel distributions conformed to a normal distribution, and the average error introduced in the diagnostic process was 10% [31].

Thus, the average measurement error falls within the range of 13%–20%. Furthermore, minor-scale disturbances would not significantly affect the measured current path in the plasma.

## V. CONCLUSIONS

In summary, this study utilized Faraday rotation to experimentally measure the 2D magnetic field distribution of single-wire Z pinches with and without preconditioning. The 2D current path under the condition of MHD instabilities was investigated. Also, the regulation process and mechanism of prepulse current on Z-pinch plasma were clarified. The preconditioning of the single-wire load significantly affects the dynamics and current distribution of the plasma. When only the main current was applied to a single silver wire, the plasma showed sausage instabilities, and the current displayed a noticeable radial component at different axial positions rather

than following the path of least inductance. Moreover, the current in the imploding region redistributed from a small to a large radius after stagnation. When the load was preconditioned, homogeneous core-coronal plasma was formed and imploded similarly to a snowplow. During the shell implosion process, the implosion velocity of the current shell exceeded that of the dense shell, consistent with simulation results. Additionally, the prepulse current can suppress and delay MRTIs by rapidly modifying the density profiles of the load.

## ACKNOWLEDGMENTS

This work was supported by the National Natural Science Foundation of China (Grants No. 51922087 and No. 51790523) and Shaanxi Provincial Science and Technology Plan Project (No. 2022TD-59 and No. 2019JCW-04).

- 
- [1] G. R. Bennett, M. E. Cuneo, R. A. Vesey, J. L. Porter, R. G. Adams, R. A. Aragon, J. A. Caird, O. L. Landen, P. K. Rambo, D. C. Rovang *et al.*, Symmetric Inertial-Confinement-Fusion-Capsule Implosions in a Double-Z-Pinch-Driven Hohlraum, *Phys. Rev. Lett.* **89**, 245002 (2002).
- [2] R. A. Vesey, M. E. Cuneo, G. R. Bennett, J. L. Porter, R. G. Adams, R. A. Aragon, P. K. Rambo, L. E. Ruggles, W. W. Simpson, and I. C. Smith, Demonstration of Radiation Symmetry Control for Inertial Confinement Fusion in Double Z-Pinch Hohlräume, *Phys. Rev. Lett.* **90**, 035005 (2003).
- [3] K. L. Baker, J. L. Porter, L. E. Ruggles, G. A. Chandler, C. Deeney, M. Vargas, A. Moats, K. Struve, J. Torres, J. McGurn *et al.*, Soft x-ray measurements of z-pinch-driven vacuum hohlraums, *Appl. Phys. Lett.* **75**, 775 (1999).
- [4] M. E. Cuneo, E. M. Waisman, S. V. Lebedev, J. P. Chittenden, W. A. Stygar, G. A. Chandler, R. A. Vesey, E. P. Yu, T. J. Nash, D. E. Bliss *et al.*, Characteristics and scaling of tungsten-wire-array z-pinch implosion dynamics at 20 MA, *Phys. Rev. E* **71**, 046406 (2005).
- [5] W. A. Stygar, M. E. Cuneo, R. A. Vesey, H. C. Ives, M. G. Mazarakis, G. A. Chandler, D. L. Fehl, R. J. Leeper, M. K. Matzen, D. H. McDaniel *et al.*, Theoretical z-pinch scaling relations for thermonuclear-fusion experiments, *Phys. Rev. E* **72**, 026404 (2005).
- [6] J. Narkis, F. Conti, and F. N. Beg, Material effects on dynamics in triple-nozzle gas-puff Z pinches, *Phys. Rev. E* **105**, 045205 (2022).
- [7] A. J. Harvey-Thompson, S. V. Lebedev, G. Burdiak, E. M. Waisman, G. N. Hall, F. Suzuki-Vidal, S. N. Bland, J. P. Chittenden, P. De Grouchy, E. Khoory *et al.*, Suppression of the Ablation Phase in Wire Array Z Pinches Using a Tailored Current Prepulse, *Phys. Rev. Lett.* **106**, 205002 (2011).
- [8] A. Lorenz, F. N. Beg, J. Ruiz-Camacho, J. Worley, and A. E. Dangor, Influence of a Prepulse Current on a Fiber Z Pinch, *Phys. Rev. Lett.* **81**, 361 (1998).
- [9] M. Li, L. Sheng, L. P. Wang, Y. Li, C. Zhao, Y. Yuan, X. J. Zhang, M. Zhang, B. D. Peng, J. H. Zhang *et al.*, The effects of insulating coatings and current prepulse on tungsten planar wire array Z-pinches, *Phys. Plasma* **22**, 122710 (2015).
- [10] J. Wu, Y. Lu, Z. Chen, D. Zhang, H. Shi, Z. Jiang, and Z. Wang, Experimental study of the dynamics of planar wire array Z-pinch preconditioned by a controlled prepulse current, *Phys. Plasma* **29**, 032702 (2022).
- [11] J. Wu, Y. Lu, F. Sun, X. Jiang, Z. Wang, D. Zhang, X. Li, and A. Qiu, Researches on preconditioned wire array Z pinches in Xi'an Jiaotong University, *Matter Radiat. Extremes* **4**, 036201 (2019).
- [12] F. J. Wessel, F. S. Felber, N. C. Wild, H. U. Rahman, A. Fisher, and E. Ruden, Generation of high magnetic fields using a gas-puff Z pinch, *Appl. Phys. Lett.* **48**, 1119 (1986).
- [13] V. V. Ivanov, J. P. Chittenden, R. C. Mancini, D. Papp, N. Niasse, S. D. Altamara, and A. A. Anderson, Investigation of plasma instabilities in the stagnated Z pinch, *Phys. Rev. E* **86**, 046403 (2012).
- [14] E. Kroupp, E. Stambulchik, A. Starobinets, D. Osin, V. I. Fisher, D. Alumot, Y. Maron, S. Davidovits, N. J. Fisch, and A. Fruchtman, Turbulent stagnation in a Z-pinch plasma, *Phys. Rev. E* **97**, 013202 (2018).
- [15] G. Sarkisov, A. Shikanov, B. Etlicher, S. Attelan, C. Rouille, and V. V. Yan'kov, Structure of the magnetic fields in Z-pinches, *Zh. Eksp. Teor. Fiz.* **108**, 1355 (1995) [*JETP Lett.* **81**, 743 (1995)].
- [16] G. Davara, L. Gregorian, E. Kroupp, and Y. Maron, Spectroscopic determination of the magnetic-field distribution in an imploding plasma, *Phys. Plasmas* **5**, 1068 (1998).
- [17] G. Sarkisov, B. Etlicher, S. Attelan, C. Rouille, and A. Shikanov, Observation of a current-loss effect at the neck of a Z-pinch formed in the explosion of a wire, *JETP Lett.* **61**, 485 (1995).
- [18] Z. Chen, J. Wu, Y. Lu, Z. Jiang, C. Zhang, Z. Wang, H. Shi, X. Li, and L. Zhou, Measurement of dynamic atomic polarizabilities of Al at 19 wavelengths from 420 nm to 680 nm in electrical exploding wire experiments, *Opt. Express* **30**, 26102 (2022).
- [19] J. Shiloh, A. Fisher, and E. Bar-Avraham, Interferometry of a gas-puff z-pinch plasma, *Appl. Phys. Lett.* **35**, 390 (1979).
- [20] G. Swadling, S. Lebedev, G. Hall, S. Patankar, N. Stewart, R. Smith, A. Harvey-Thompson, G. Burdiak, P. de Grouchy, and J. Skidmore, Diagnosing collisions of magnetized, high energy density plasma flows using a combination of collective

- Thomson scattering, Faraday rotation, and interferometry, *Rev. Sci. Instrum.* **85**, 11E502 (2014).
- [21] Z. Jiang, J. Wu, Z. Chen, Z. Wang, H. Shi, and X. Li, Improved measurement method for the Faraday rotation distribution using beam splitting, *Opt. Express* **30**, 8917 (2022).
- [22] N. R. Pereira, N. Rostoker, and J. S. Pearlman, Z-pinch instability with distributed current, *J. Appl. Phys.* **55**, 704 (1984).
- [23] G. Pretzler, A new method for numerical Abel-inversion, *Z. Naturforsch., A: Phys. Sci.* **46**, 639 (1991).
- [24] A. L. Velikovich, F. L. Cochran, and J. Davis, Suppression of Rayleigh-Taylor Instability in Z-Pinch Loads with Tailored Density Profiles, *Phys. Rev. Lett.* **77**, 853 (1996).
- [25] A. G. Rousskikh, A. S. Zhigalin, V. I. Oreshkin, N. A. Labetskaya, S. A. Chaikovskiy, A. V. Batrakov, G. Y. Yushkov, and R. B. Baksht, Study of the stability of Z-pinch implosions with different initial density profiles, *Phys. Plasma* **21**, 052701 (2014).
- [26] J. Wu, Y. Lu, X. Li, D. Zhang, and A. Qiu, Investigations on stratification structure parameters formed from electrical exploding wires in vacuum, *Phys. Plasmas* **24**, 112701 (2017).
- [27] J. J. MacFarlane, I. E. Golovkin, and P. R. Woodruff, HELIOS-CR—A 1-D radiation-magnetohydrodynamics code with inline atomic kinetics modeling, *J. Quant. Spectrosc. Radiat. Transfer* **99**, 381 (2006).
- [28] G. Rosenzweig, E. Kroupp, T. Queller, A. Starobinets, Y. Maron, V. Tangri, J. L. Giuliani, and A. Fruchtman, Local measurements of the spatial magnetic field distribution in a z-pinch plasma during and near stagnation using polarization spectroscopy, *Phys. Plasmas* **27**, 022705 (2020).
- [29] V. V. Ivanov, A. A. Anderson, D. Papp, A. L. Astanovitskiy, V. Nalajala, and O. Dmitriev, Study of magnetic fields and current in the Z pinch at stagnation, *Phys. Plasmas* **22**, 092710 (2015).
- [30] V. V. Ivanov, A. A. Anderson, and D. Papp, Investigation of wire-array Z-pinches by laser probing diagnostics, *Matter Radiat. Extremes* **4**, 017401 (2019).
- [31] Z. Jiang, J. Wu, Z. Chen, W. Wang, Z. Wang, Y. Lu, H. Shi, X. Li, and A. Qiu, Improvement of Faraday rotation and its application in preconditioned single-wire Z-pinch plasma, *IEEE Trans. Plasma Sci.* **51**, 944 (2023).